ADVANCED ENERGY MATERIALS
www.advenergymat.de

Graphene-Based Sulfur Cathodes and Dual Salt-Based Sparingly Solvating Electrolytes: A Perfect Marriage for High Performing, Safe, and Long Cycle Life Lithium-Sulfur Prototype Batteries

Julen Castillo, Asier Soria-Fernández, Sergio Rodriguez-Peña, Jokin Rikarte, Adrián Robles-Fernández, Itziar Aldalur, Rosalía Cid, Jose Antonio González-Marcos, Javier Carrasco, Michel Armand, Alexander Santiago, and Daniel Carriazo*

The growing requirements for electrified applications entail exploring alternative battery systems. Lithium-sulfur batteries (LSBs) have emerged as a promising, cost-effective, and sustainable solution; however, their practical commercialization is impeded by several intrinsic challenges. With the aim of surpassing these challenges, the implementation of a holistic LSB concept is proposed. To this end, the effectiveness of coupling a high-performing 2D graphene-based sulfur cathode with a well-suited sparingly solvating electrolyte (SSE) is reported. The incorporation of bis(fluorosulfonyl)imide (LiFSI) salt to tune sulfolane and 1,1,2,2-tetrafluoroethyl-2,2,3,3-tetrafluoropropylether based SSE enables the formation of a robust and compact lithium fluoride-rich solid electrolyte interphase. Consequently, the lithium compatibility is improved, achieving a high Coulombic efficiency (CE) of 98.8% in the Li||Cu cells and enabling thin and dense lithium depositions. When combined with a high-performing 2D graphene-based sulfur cathode, a symbiotic effect is shown, leading to high discharge capacities, remarkable rate capability (2.5 mAh cm^{-2} at C/2), enhanced cell stability, and wide temperature applicability. Furthermore, the scalability of this strategy is successfully demonstrated by assembling high-performing monolayer prototype cells with a total capacity of 93 mAh, notable capacity retention of 70% after 100 cycles, and a high average CE of 99%.

1. Introduction

The increasing demand for new electrified applications underscores the crucial importance of the development of new energy storage technologies.[1,2] So far, this demand has been met by lithium-ion batteries (LIBs), which have pervaded the rechargeable battery market since their commercialization in the 1990s.[3,4] However, the growing energy density requirements for some applications such as transportation, exceed the capabilities of current commercial LIBs.[5–7] This, together with the concerns related to the supply chain, high cost, and sustainability issues associated with many materials used in conventional LIBs like nickel or cobalt, further emphasizes the need for the development of new sustainable and potentially cost-effective rechargeable battery technologies.[8,9] In this context, lithium-sulfur batteries (LSBs) are emerging as a promising and viable alternative among

J. Castillo, A. Soria-Fernández, S. Rodriguez-Peña, J. Rikarte, A. Robles-Fernández, I. Aldalur, R. Cid, J. Carrasco, M. Armand, A. Santiago, D. Carriazo
Centre for Cooperative Research on Alternative Energies (CIC energiGUNE)
Basque Research and Technology Alliance (BRTA)
Vitoria-Gasteiz 01510, Spain
E-mail: asantiago@cicenergigune.com

J. Castillo, S. Rodriguez-Peña, J. A. González-Marcos
University of the Basque Country (UPV/EHU)
Barrio Sarriena, s/n, Leioa 48940, Spain

J. Carrasco, D. Carriazo
IKERBASQUE, Basque Foundation for Science
Plaza Euskadi 5, Bilbao 48009, Spain

The ORCID identification number(s) for the author(s) of this article can be found under https://doi.org/10.1002/aenm.202302378

DOI: 10.1002/aenm.202302378

the different next-generation battery technologies owing to the excellent properties that their operating chemistry offers.[10] Apart from the low cost, wide availability, and environmental friendliness of sulfur as active material, its outstandingly high theoretical specific energy (up to 2600 Wh kg^{-1}) makes LSBs an ideal technology for weight-critical applications, such as heavy automotive vehicles, aviation, high-altitude pseudo satellites (HAPS), high-altitude long endurance (HALE) vehicles or electric vertical take-off and landing (eVTOL) aircraft.[9,11–13]

Despite its potential benefits, the development of LSB technology has encountered significant challenges since its discovery in the 1960s, posing obstacles to its successful commercialization.[14–16] Some of the main issues to be addressed include the insulating nature of both the initial product (elemental sulfur, S_8) and the end-products (Li_2S_2 and Li_2S), the dissolution of the intermediate components (lithium polysulfides, LiPS) into the electrolyte that causes the loss of active material and the poisoning of the lithium anode (commonly referred as "shuttle effect"), and the substantial volume expansion experienced by the positive electrode after complete lithiation of sulfur to Li_2S (up to 80%).[17–21]

Over the past decades, a tremendous research effort has been carried out to address these challenges. For instance, academia has put special interest in the screening and development of the carbonaceous material used for the design of the sulfur cathode, since it is of paramount importance to mitigate the abovementioned issues.[22–25] In this line, our group has reported the outstanding sulfur utilization and partial retention of polysulfides provided by 2D graphene-based activated carbons, used both as a carbon to maximize the performance of LSBs even at prototype scale.[15,26]

Nevertheless, despite the multiple benefits of these carbon materials, using them as the only improvement strategy is not enough to solve other important operational problems that emerge during LSB cycling, such as the degradation of the lithium metal anode (LMA) and electrolyte depletion.[9,27] These issues are usually masked under laboratory conditions, as the active material loading and/or the electrolyte amount are not optimized. However, when attempting to replicate industry-specific conditions, such issues emerge, especially during the upscaling process to prototype cells.[12,14,26–29] Regrettably, the prevailing strategy has been to tackle the immediate problems using a singular approach, disregarding the broader spectrum of challenges that demand resolution. In other words, rather than adopting the industry's imperative for a holistic research effort, the focus has remained narrow and incomplete.

On the other hand, through the electrolyte engineering strategy, great strides are currently being made in modifying and developing new electrolyte systems.[30–32] This essential component can be envisaged as the lifeblood of the battery, playing a key role in the correct operation and ensuring the long-term stability of a battery due to its interaction with the LMA. Ether-based electrolyte comprising lithium bis(trifluoromethanesulfonyl)imide (LiTFSI) salt dissolved in a solvent mixture based on 1,2-dimethoxyethane (DME) and 1,3-dioxolane (DOL) in an equal volumetric ratio, and lithium nitrate ($LiNO_3$) as solid electrolyte interphase (SEI) promotor additive, has been widely employed as the conventional electrolyte for LSBs.[32–34] Despite the good properties in terms of ionic conductivity and high sulfur utilization, it proved to be unable to guarantee long-term cycling, particularly under practical operating conditions.[15,27,34] Their use results in a battery system based on the dissolution-precipitation mechanism, which leads to the dissolution of a significant amount of LiPS, thereby facilitating their migration to the Li anode and ultimately culminating in the aforementioned "shuttle effect". This unwanted process aggravates the stability issues of the electrolyte accelerating the $LiNO_3$ depletion by its interaction with the dissolved LiPS. In summary, decreasing the amount of electrolyte in this system is a real challenge, as enough quantity is required to ensure the smooth occurrence of dissolution/precipitation-based reaction pathways.[35,36]

In light of the operational issues of the conventional electrolyte, in recent years sparingly solvating electrolytes (SSEs), also known as localized or diluted high concentrated electrolytes (LHCEs or DHCEs, respectively), have recently emerged as an appealing alternative for their practical application in LSBs.[37–39] These types of electrolytes not only reduce or inhibit the dissolution of LiPS by shifting the battery operation to a quasi-solid state reaction mechanism system but also possess a unique solvation structure and remarkable physicochemical properties that enable the correct regulation of lithium deposition.[38] SSEs are formed according to the highly concentrated electrolytes (HCEs) concept, in which the increased amount of salt results in the reduction of free solvent molecules in the electrolyte and greatly improves the stability against the LMA.[40,41] Nevertheless, the application of HCE in batteries is hampered due to their high viscosity, low ionic conductivity, and high cost associated with the high amount of lithium salt employed.[42,43] In this sense, the incorporation of hydrofluoroethers (HFEs) as diluents, which are miscible with the electrolyte solvents but do not dissolve lithium salt due to their low donor number, overcome these limitations while maintaining the excellent properties of HCEs.[44] As has been widely reported in lithium-metal batteries (LMBs), SSEs demonstrate remarkable compatibility with LMA. This is due to their distinguished solvation structure, which promotes the formation of a protective SEI layer that is primarily created from the decomposition products of lithium salt anions rather than organic solvents, owing to the higher presence of contact ion pairs (CIPs) and cation-anion aggregates (AGGs).[45–47] This change results in the formation of an inorganic-rich SEI layer that effectively prevents parasitic reactions between the electrolyte and the LMA. Therefore, the proper selection of the lithium salt anion is critical. As a result, LMBs have leveraged the unique solvation properties of these electrolytes by employing bis(fluorosulfonyl)imide (LiFSI) as main salt, which leads to the formation of a lithium fluoride (LiF)-rich SEI protective layer,[6,48,49] or by utilizing $LiNO_3$ to create an N-rich SEI layer.[50,51] The approach of the appropriate selection of lithium salt has led to substantial enhancement in battery stability, even under realistic operating conditions. However, in the case of LSBs, due to the inherent limitations of a technology based on conversion reactions, the potential impact of lithium salt on SEI formation has not been fully exploited and LiTFSI has commonly been used as the unique lithium salt. Despite the good properties in terms of thermal and chemical stability and high ionic conductivity that LiTFSI presents, due to its highly stable anion molecule, the protective layer formed is usually less functional than in the case of LiFSI or $LiNO_3$.

In this study, we aim to address the current challenges and boost the commercialization of LSBs by implementing a comprehensive battery design approach. Our proposal involves integrating multiple strategies based on the holistic battery concept, enabling us to effectively overcome existing obstacles. To this end, we propose the combination of sulfur cathodes constructed using a graphene-based activated carbon, which has been developed by our research group, with the utilization of SSEs, further enhancing the battery's performance. Two different SSEs were developed during the study, both based on a combination of sulfolane (SL) as solvent and 1,1,2,2-tetrafluoroethyl-2,2,3,3-tetrafluoropropylether (TTE) as co-solvent. The first electrolyte, named SSE_REF, was completed with LiTFSI as the unique lithium salt while the second electrolyte (SSE_LiFSI) studies the combination of LiTFSI and LiFSI considering that the latter salt can act as LiF-rich SEI layer precursor. The proposed SSEs are thoroughly characterized in terms of their physicochemical and electrochemical properties. In addition, classical molecular dynamics (MD) simulations were performed to analyze the solvation structure of these electrolytes. The flammability test was evaluated as a key criterion for assessing the safety of the battery system. Subsequently, the compatibility of these electrolytes with the lithium anode has been extensively evaluated through various tests such as Li/Cu cells to determine their Coulombic efficiency (CE), galvanostatic cycling of Li||Li symmetric cells, and critical current density (CCD) test. The electrochemical properties of the electrolytes are further characterized in practical Li-S coin cells. Finally, the feasibility of scaling the holistic approach is successfully demonstrated through the fabrication of 20 cm^2 pouch cells.

2. Results and Discussion

As previously mentioned, this study focuses on the implementation of a holistic approach to LSBs, achieved through the combination of a previously reported high-performing 2D graphene-based sulfur cathode[26] and a newly developed SSE that was fine-tuned during the course of this work, and which will be referred to as SSE_LiFSI for the remainder of this discussion. To evaluate its performance, this new SSE was compared against both conventional DME/DOL electrolyte and a reference SSE electrolyte (SSE_REF). **Figure** 1a compiles the ionic conductivities of the tested electrolytes at room temperature (i.e., 23 ± 2 °C). The conventional DME/DOL electrolyte exhibits the highest ionic conductivity of 6.47 mS cm^{-1}, which is approximately three times higher than that of the prepared SSEs. This difference can primarily be attributed to the lower viscosity of the DME/DOL electrolyte as well as the lower concentration of solvated salt by the solvent molecules. Nevertheless, the two SSEs present sufficiently high ionic conductivities of 1.21 and 2.08 mS cm^{-1} for SSE_REF and SSE_LiFSI, respectively, enough to ensure reliable battery operation. It is worth noting a slight difference between SSE_LiFSI and SSE_REF, which can be attributable to the increased mobility of the smaller LiFSI molecules. Furthermore, a wettability study conducted on the Celgard 2500 separator confirms the higher viscosity of SSEs. The conventional electrolyte, formed by low viscosity and high volatility solvents, presents an excellent wettability of the separator (contact angle of 31°) attributed to its lower viscosity (Figure 1b–d). In contrast, both SSEs exhibited lower wetting properties of the separator (67° and 54° for SSE_REF and SSE_LiFSI, respectively), primarily due to the higher viscosity of SL employed for their preparation, as corroborated by the viscosity measurements shown in Figure S1 (Supporting Information).

MD simulations were performed to gain atomistic-level insights into the solvation structure of the prepared electrolytes and the effect of the co-solvent incorporation on the microscopic structure of the Li salt/SL mixtures. The snapshots illustrating the chemical structure of the different electrolytes after reaching thermodynamic equilibrium are presented in Figures 1e–g and Figure S2 (Supporting Information). To compare the solvation structures, radial distribution functions (g(r), represented by solid lines) and coordination numbers (n(r), indicated by dash-point lines) were calculated, as observed in Figures 1f,h. The DME/DOL electrolyte predominantly exhibits a higher fraction of solvent-separated ion pairs (SSIPs) structures, indicated by the lower coordination number value of Li-O_{TFSI}, where the coordination of Li^+ is mainly governed by DME and NO_3^-. The sharp radial distribution function peak observed for NO_3^-, compared with the relatively low peak of DME, underscores that while NO_3^- is consistently coordinated with the Li^+, there are many DME molecules not coordinated with it as illustrated in Figure 1e. In Figure S3a (Supporting Information), an illustrative representation of Li^+ coordination is shown, highlighting the role of NO_3^- as a connecting bridge between various Li^+ ions, forming the aggregations depicted in Figure 1e. Conversely, in both SSEs, a distinct Li-O_{SL} peak at ≈2 Å, together with Li-O_{TFSI} and Li-O_{FSI} peaks, are identified, indicating that the lithium salts (LiTFSI for SSE_REF and both LiTFSI and LiFSI in the case of SSE_LiFSI) are surrounded by the SL solvent molecules within the first coordination shell. Examples of these can be found in Figures S3b,c (Supporting Information). Similarly to NO_3^- in DME_DOL electrolyte, TFSI, and FSI serve to connect different Li^+ and form the aggregates observed in Figure 1g and Figure S2a (Supporting Information). In contrast, the TTE molecules display negligible coordination with Li^+. Therefore, this clearly demonstrated that both prepared SSEs exhibit localized concentrations of Li salt/SL pairs. These are surrounded by TTE molecules that primarily act as diluents without being involved in the solvation structures of Li^+.

The solvation structures of the developed SSEs were confirmed by Raman spectroscopy. Figure 1i displays the Raman spectra SO_2 scissoring vibration of sulfolane within the corresponding spectra range. In pure sulfolane, this peak appears at 568 cm^{-1} and undergoes a shift toward higher wavenumber upon complexation with Li^+, as observed by increasing salt concentration in the electrolyte, reflecting the reduction of the free SL solvent molecules. Interestingly, this displacement is independent of the type of lithium salt used in the electrolyte, being this trend similarly observed in both developed electrolytes.

Additionally, it is worth focusing on the spectral region between 740 and 750 cm^{-1}, which is associated with the CF_3 bending coupled with the S–N stretching vibration of the TFSI anions. In the same region but at slightly lower Raman shifts (730–740 cm^{-1}), the vibrations related to the stretching of S—N moieties of the FSI anions are found. These particular vibrational modes are known for their sensitivity to variations in Li-ion coordination (Figure 1j). When the compound is uncoordinated, as in the case of low-concentration electrolytes, the Raman peak in

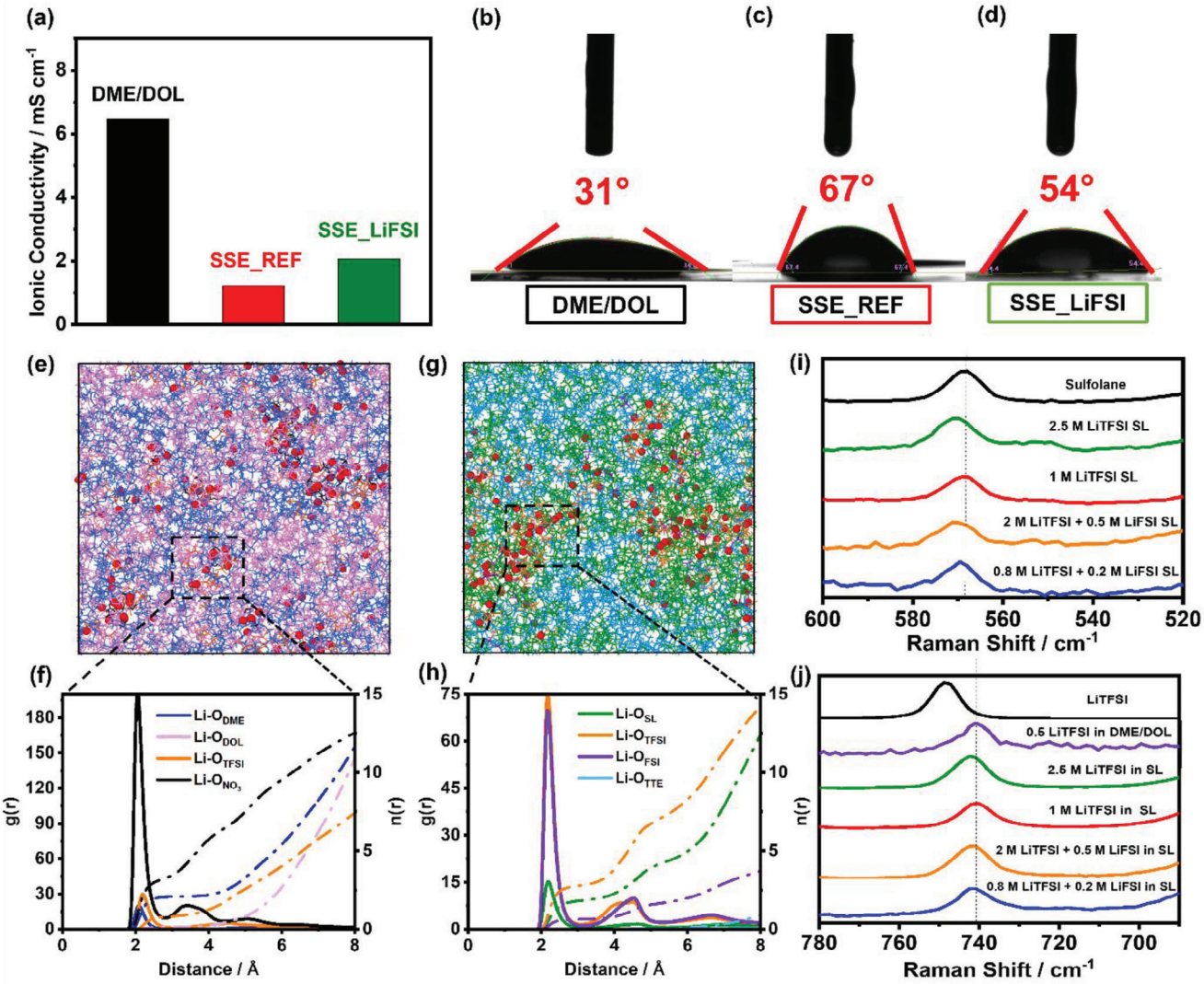

Figure 1. Individual properties and electrolyte solvation structures: a) Ionic conductivity of the studied electrolytes measured at room temperature (23 ± 2 °C). Wettability test on Celgard separator of b) DME/DOL, c) SSE_REF, and d) SSE_LiFSI. MD simulation snapshots and radial distribution function of e) and f) DME/DOL and g) and h) SSE_LiFSI. Raman spectra of different configurations of electrolytes for varied i) sulfolane and j) LiTFSI salt ranges.

this region shifts to shorter wavelengths, especially ≈740 cm^{-1}. However, as the salt concentration in the system increases, the formation of CIPs or AGGs occurs appearing a new peak in the spectra at ≈747 cm^{-1} (see deconvoluted spectra of concentrated electrolytes in Figure S4, Supporting Information), leading to a shift of the band toward longer wavelengths. This shift from 740 to 742 cm^{-1} of the main peak of LiTFSI could indicate the possible monodentate coordination between $TFSI^-$ and Li^+. In the case of the electrolytes containing FSI anion in their composition, a new peak at 734 cm^{-1} can be found.[52] The observed band shifts in the analyzed spectra suggest that the developed electrolytes in this work present the formation of CIPs and AGGs by the anions of the salts.

Liquid electrolytes have long been criticized for their high flammability, which would eventually lead to well-known safety incidents. Consequently, ensuring fire safety is of paramount importance in the development of secure battery systems, which are closely intertwined with the combustion characteristics and thermal stability of the employed electrolytes. To evaluate the safety level of the developed electrolytes, a flammability test was conducted. **Figure** 2a–c displays the digital photos captured during the flammability test, where the commercial Celgard separator was soaked in the respective electrolytes. Remarkably, the conventional DME/DOL electrolyte presents highly flammable behavior, evident from its easy ignition and violent combustion, resulting in complete combustion of the Celgard within just 1 s. In contrast, neither of the two SSEs show any signs of catching fire, evidence of their exceptional resistance to combustion. The Celgard separator only experiences slight melting in some areas, likely due to the higher temperature of the lighter flame exceeding the melting point of the material. Additionally, as shown in Figure S5 (Supporting Information), the flammability test of the

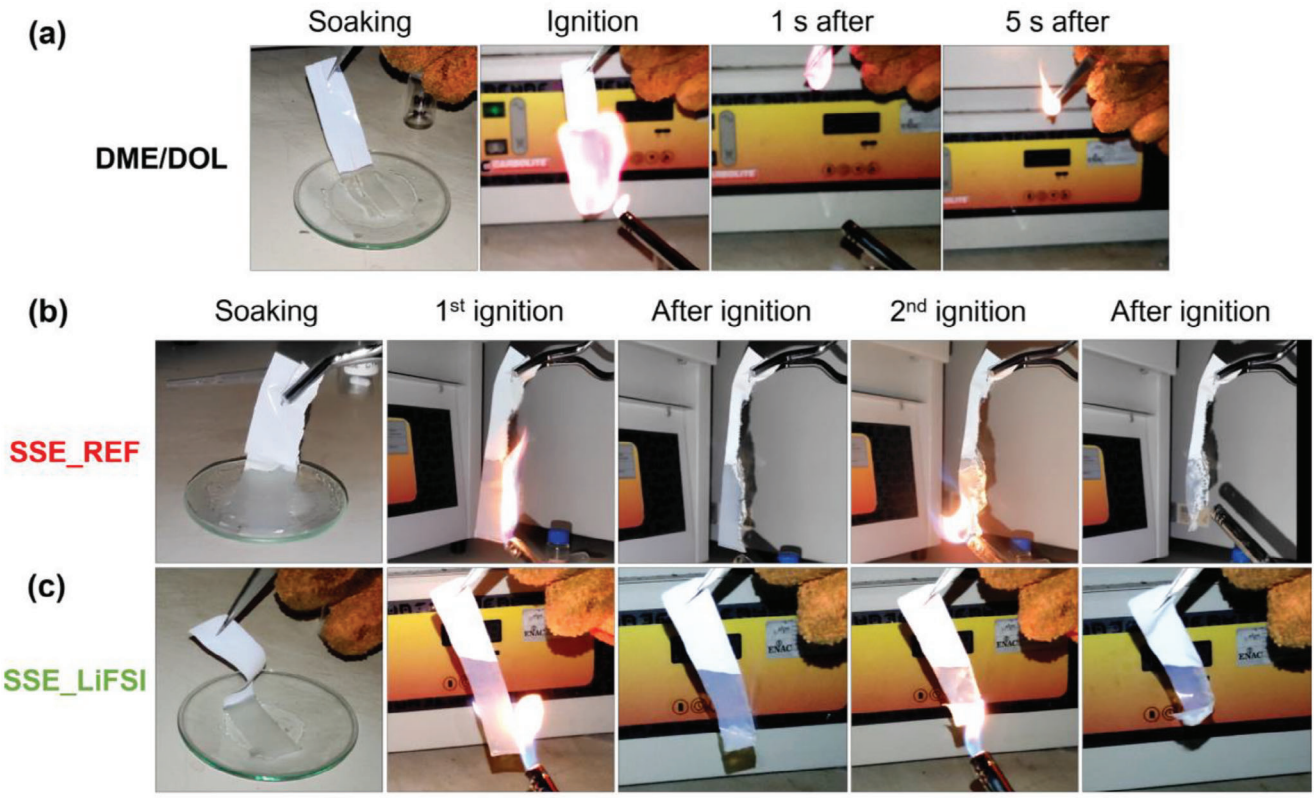

Figure 2. Flammability test of the Celgard separator soaked in different electrolytes. The digital photos of the burning process of a) DME/DOL, b) SSE_REF, and c) SSE_LiFSI.

electrolytes was conducted to quantify their flame-retardant rate through the self-extinguishing time (SET) values. Once again, the low thermal stability and susceptibility to combustion of the conventional DME/DOL electrolyte are evidenced by its vigorous flame, resulting in a SET value of 117 s g^{-1}. Indeed, both SSEs continue to demonstrate their non-flammable nature, reflecting a negligible SET value. Hence, the replacement of the flammable conventional electrolyte with the prepared SSEs will significantly enhance the fire safety properties of the battery system.

In addition to the intrinsic properties, the compatibility of the electrolyte with LMA is a key requirement for ensuring long-term LMB cycling. Hence, a deep study of the reversibility and stability of the LMA during the plating and stripping process in the developed electrolytes was assessed using different Li||Cu and Li||Li cell tests represented in **Figures 3–5**. First, the lithium plating and stripping cycling in Li||Cu cells at 0.5 mA cm^{-2} was performed in order to evaluate the CE obtained through this study (Figure S6, Supporting Information). Figure 3a demonstrates the excellent stability of the SSE_LiFSI electrolyte, evidenced by a plating/stripping average CE value of 97% during the analyzed cycles. Notably, there is a significant stability contrast when compared to the SSE_REF electrolyte, which fails to yield an acceptable CE value (<80%) due to different side reactions. In addition, as depicted in Figure 3b and Figures S7 and S8a (Supporting Information), SSE_LiFSI presents lower polarization voltage compared to SSE_REF, without showing any cycling failure sign. Therefore, the substantial stability improvement resulting from the introduction of the LiFSI salt into the system for the SSE preparation is highlighted. On the other hand, as expected, the conventional DME/DOL electrolyte displays high CE values during cycling and low polarization voltage (Figure S8b, Supporting Information), mainly attributed to the protective and denser lithium deposition properties provided by the $LiNO_3$ additive.

As a complementary study to determine the CE of LMA in Li||Cu cells, the modified Aurbach method was performed.[53] This method differs from the previous one as it incorporates a preconditioning step of the Cu substrate (see Experimental Section). As can be observed in Figure S9 (Supporting Information), the SSE_REF shows again the worst compatibility against lithium with a low CE of 58.1%. This incompatibility is solved by the addition of LiFSI in SSE_LiFSI electrolyte, as presented in Figure 3c where the results of the DME/DOL and SSE_LiFSI electrolytes are displayed, demonstrating the suitable properties of this salt in generating a robust SEI layer, resulting in a CE of 98.8%. Notably, this CE value is even higher than that calculated for the conventional DME/DOL-based electrolyte (95.2%). Regarding the plating/stripping profiles, despite exhibiting a slightly lower CE, the conventional electrolyte displays a lower overpotential than SSE_LiFSI (Figure 3c). This can be attributed to the higher ionic conductivity of the electrolyte and the formation of an N-rich SEI protective layer facilitated by $LiNO_3$ in contrast to the insulator LiF-rich SEI layer formed in the SSE_LiFSI system. The validity of the aforementioned description is supported by Figure 3d and Figure S10 (Supporting Information), which

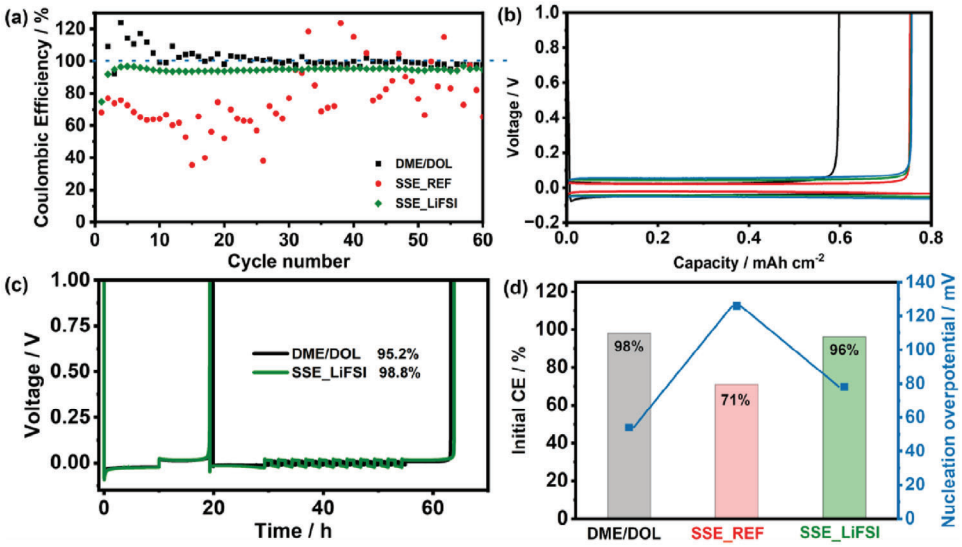

Figure 3. Electrochemical compatibility with LMA of the studied electrolytes. a) Coulombic efficiency of the cycling performance of Li||Cu cells employing different electrolytes. b) Polarization of SSE_LiFSI during the Li plating and stripping in Li||Cu cells. c) Li metal CE of the different electrolytes using the modified Aurbach method.[52] d) CE and nucleation overpotential of the first lithium deposition.

confirm the high compatibility of the SSE_LiFSI electrolyte with lithium. The compatibility is found to be comparable to that of the conventional electrolyte. The CE is nearly identical for both DME_DOL and SSE_LiFSI electrolytes, although the former exhibits lower nucleation overpotential, improving in both cases the performance obtained with SSE_REF.

Continuing the study of the compatibility of the different electrolytes with LMA, surface and cross-section morphologies of the first lithium deposition on Cu were examined by scanning electron microscopy (SEM) analysis (Figure 4a; Figure S11, Supporting Information). Conventional DME/DOL electrolyte exhibits a compact lithium deposition film thickness of 50 µm with large particle size (Figure S11a, Supporting Information), evidencing good compatibility between the lithium and the electrolyte in the first Li deposition. In contrast, in the case of the SSE_REF electrolyte, the deposited lithium film presents a porous and poorly dense shape with a loosely packed structure with an average thickness of ≈80 µm (Figure S11b, Supporting Information). This morphology further highlights the unsuitable compatibility of this electrolyte with Li. Interestingly, SSE_LiFSI yields a larger particle size as well as a tightly denser and smoother lithium deposition, leading to a compact and thin film of ≈25 µm (Figure S11c, Supporting Information). This dense lithium deposition reduces the available surface area for interacting with the electrolyte, resulting in higher CE values as previously demonstrated. It is worth noting that, even after 30 cycles, there is only a slight increase in surface porosity, and the SSE_LiFSI still maintains large and dense lithium depositions (as shown in Figure S12, Supporting Information), in contrast to the conventional electrolyte where more fibrillar and whisker-like structures begin to emerge upon cycling.

XPS analyses were conducted to study the surface chemistry of the lithium deposition using different electrolytes. The wide-scan XPS spectra of the Li deposition surface on the Cu substrate with different electrolytes can be found in Figure S13 (Supporting Information), and their corresponding atomic content of different elements is presented in Table S1 (Supporting Information). The surface of Li^0 deposits with SSE_LiFSI presents a higher proportion of LiF compound than when SSE_REF and DME/DOL are employed, ascribed to the stronger interaction of LiFSI with Li^0 due to the weaker S—F bond (Figure 4b). The XPS results, together with the SEM images, demonstrate that the addition of a certain amount of LiFSI enables the formation of a more compact and denser lithium deposition with an interface that is richer in LiF (peak at 685 eV in F 1s core level). Moreover, it is worth noting that a qualitative and quantitative difference in the O content within the SEI layer is observed between SSE_REF and the other electrolytes. On the one hand, SSE_REF produces a SEI with lower O content (almost 24%) compared to DME/DOL and SSE_LiFSI (≈29% and 31%, respectively, see Figure S13 (Supporting Information)). On the other hand, the additional O content in DME/DOL and SSE_LiFSI electrolytes seems to be of a different nature, as suggested by the distinctive shape of the O 1s spectra (Figure S14a, Supporting Information). Notably, the visible peak at 528.6 eV when using DME/DOL and particularly SSE_LiFSI electrolytes indicates the presence of Li_2O in the SEI, whereas only a small amount is distinguished when SSE_REF is employed. Alongside the increase in Li_2O, the peak at ≈531.5 eV (mainly comprising carbonates and hydroxides) shifts to slightly lower binding energies and becomes the dominant component. Furthermore, analysis of the Li 1s core level also reveals a qualitative difference between the case of SSE_REF and the other two electrolytes. The deconvolution of Li 1s (Figure S14b, Supporting Information) spectra demonstrates that the formation of LiOH (component at 54.7 eV) is responsible for the increase and shift of the peak at 531.5 eV when DME/DOL and SSE_LiFSI electrolytes are used. Hence, the formation of Li_2O and LiOH seems to contribute to the development of a more benign interface when employing SSE_LiFSI and DME/DOL electrolytes. Finally, the appearance of a distinct peak corresponding to metallic lithium

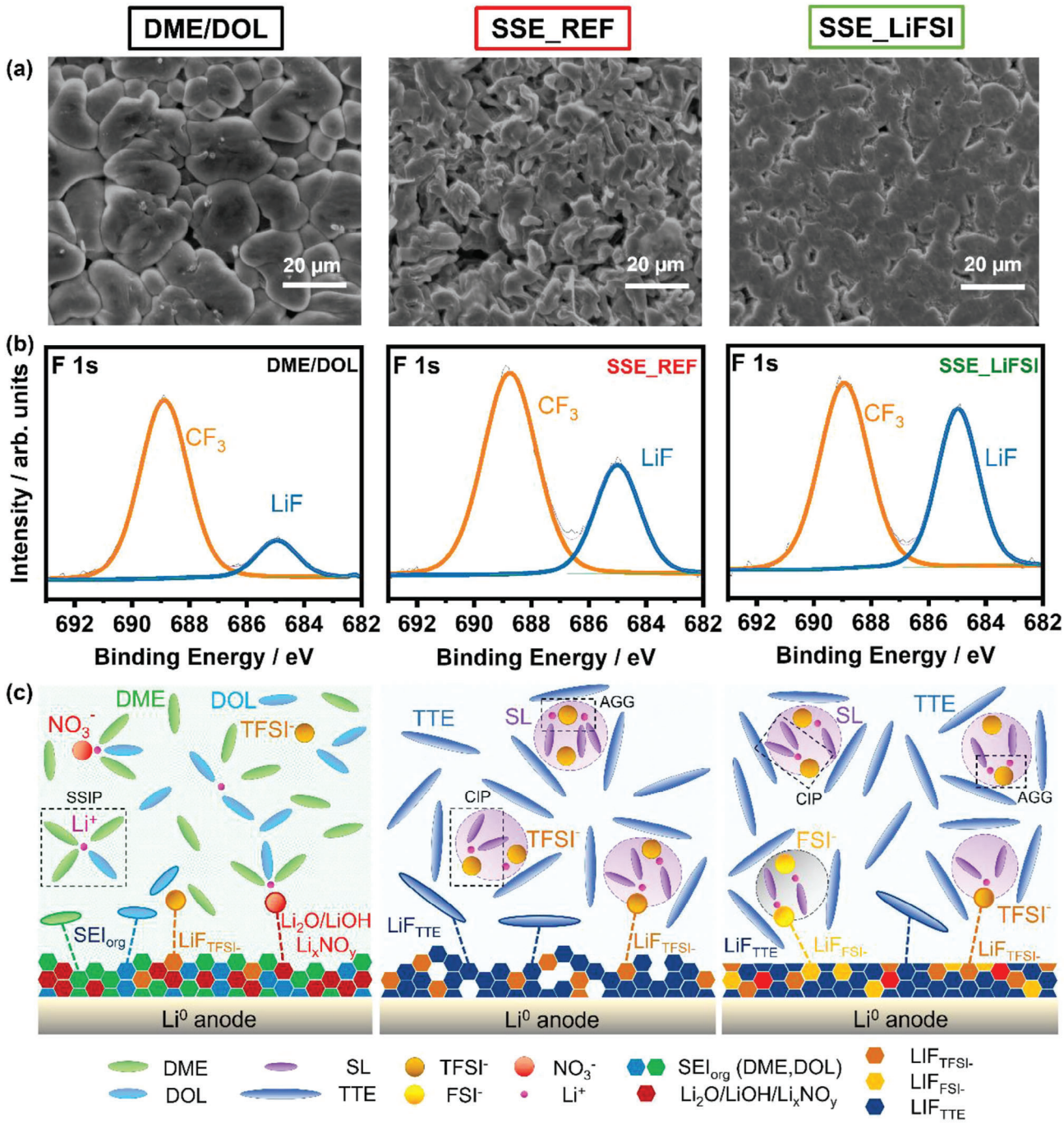

Figure 4. The morphologies, corresponding XPS surface analyses, and design principle of the first Li deposition behavior. a) SEM images of the lithium deposition on Cu foil with three different electrolytes: DME/DOL, SSE_REF, and SSE_LiFSI electrolytes. b) High-resolution XPS spectra of F 1s of the lithium deposition on Cu substrate with different electrolytes. c) Schematic illustration of the electrolyte structure and the correspondingly formed SEI in DME/DOL, SSE_REF, and SSE_LiFSI electrolytes (where SSIP, CIP, and AGG refer to solvent-separated ion pair, contact ion pair and cation-anion aggregates structure abbreviation, respectively).

(signal at 51.8 eV in Li 1s) with SSE_REF and DME/DOL electrolytes may indicate a non-compact, inhomogeneous, or extremely thin SEI in those cases (thin enough in some parts to allow collecting photoelectrons from the buried lithium metal platted), while the dense and compact lithium deposits with SSE_LIFSI are covered by an also compact and protective SEI. This compact and chemically more benign interface could explain the good compatibility of the developed electrolyte with lithium metal explained previously. Based on the results obtained in SEM and XPS analyses, schematic depictions of the SEI

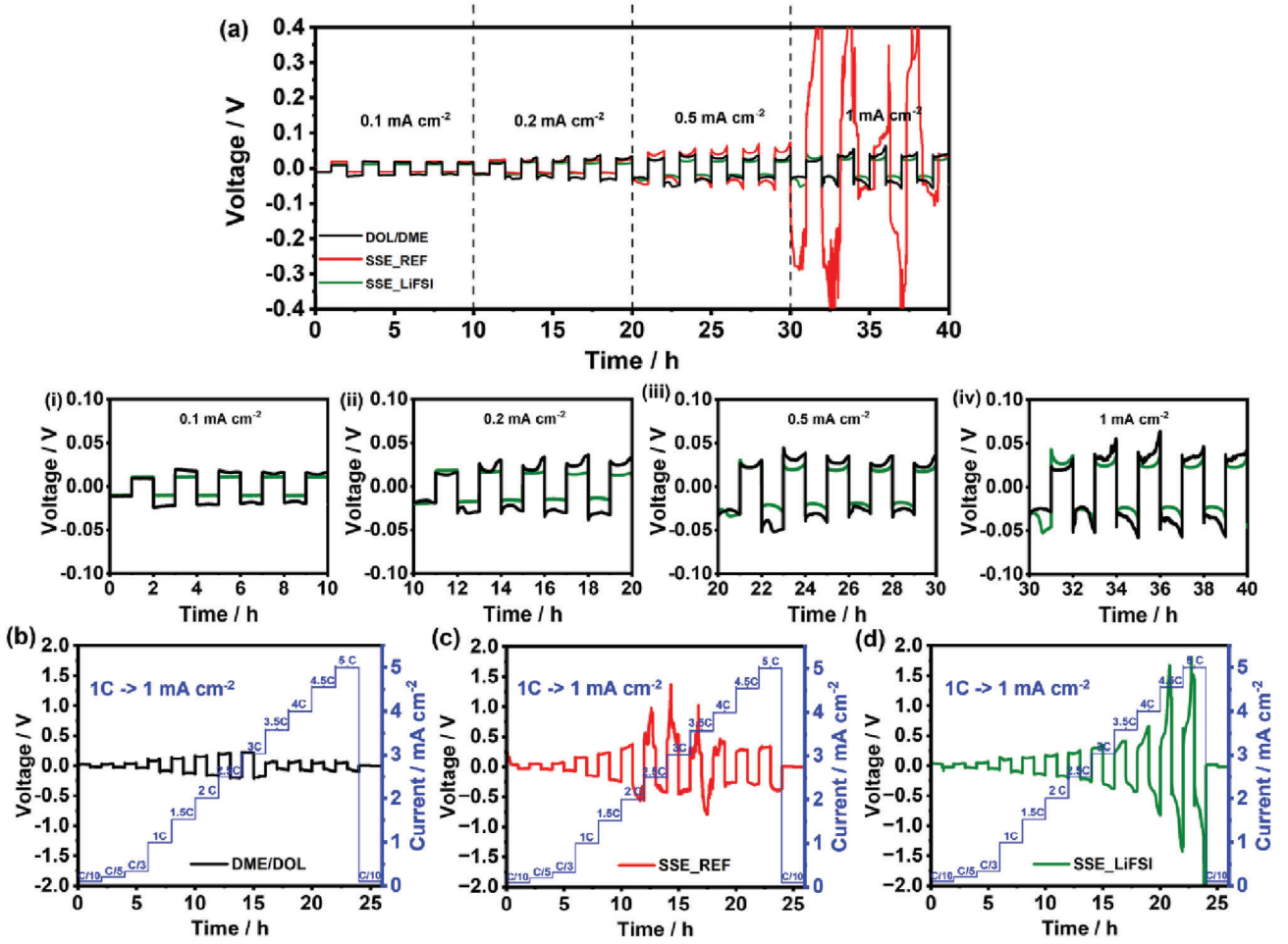

Figure 5. Electrochemical performance of different electrolytes in Li||Li cells. a) current test of Li||Li cells using DME/DOL and SSE_LiFSI electrolytes at different current densities from 0.1 to 1 mA cm^{-2} and their corresponding zoomed profiles. The critical current density of Li||Li cells using the different electrolytes: b) DME/DOL, c) SSE_REF, and d) SSE_LiFSI.

layer formation depending on the employed electrolyte after the lithium plating are presented in Figure 4c. The addition of LiFSI as an additive in the SSEs enhances the quality of the formed SEI compared to the SSEs based solely on LiTFSI. As demonstrated, this improvement is attributed to the higher decomposition of LiFSI, resulting in a greater proportion of LiF within the SEI layer. Additionally, the morphology and compactness of the lithium deposition are also influenced by the presence of LiFSI in the SSE.

To complete the electrochemical characterization of the different electrolytes, their stability at different current densities from 0.1 to 1 mA cm^{-2} was tested in a Li||Li symmetric cell (Figure 5a). This test serves as additional proof of the instability of the SSE_REF electrolyte, as previously observed. This unsatisfactory performance can be primarily attributed to irregular and fibrillar lithium deposition. In contrast, both SSE_LiFSI and DME/DOL electrolytes exhibit a flat and stable cycling behavior with minimal polarization across all current steps. This further endorses the influence of the denser and more homogeneous lithium deposition evidenced in these two electrolytes. However, it should be noted that DME/DOL electrolyte does exhibit some erratic cycles, particularly at high current densities. This behavior may be attributed to the increasing deposition porosity mentioned earlier. Noteworthy, when examining the voltage profiles in detail, SSE_LiFSI consistently displays lower overpotential throughout all current steps. This can be ascribed to its compact and thinner deposition film behavior, as discussed previously.

As a complementary study to the plating/stripping analysis, the critical current density (CCD) of the studied electrolytes was evaluated. This parameter holds significant importance in the application of electrolytes in LSBs, as it provides insights into the rate-determining steps of lithium metal kinetics and ensures the compatibility of the lithium metal interface with specific current densities and capacities. Therefore, it is essential to determine the suitability of the electrolyte for high-power applications. As shown in Figure 5b–d, the previously observed trend persists. The SSE_LiFSI electrolyte, with its robust and compact deposition characteristic, exhibits a higher resistance to current density, even up to 4 mA cm^{-2}, surpassing the performance of all other studied electrolytes. At this current density of 4 mA cm^{-2}, some inhomogeneous deposition of Li starts to appear and, as a consequence, the shape of the plateaus turns irregular. Con-

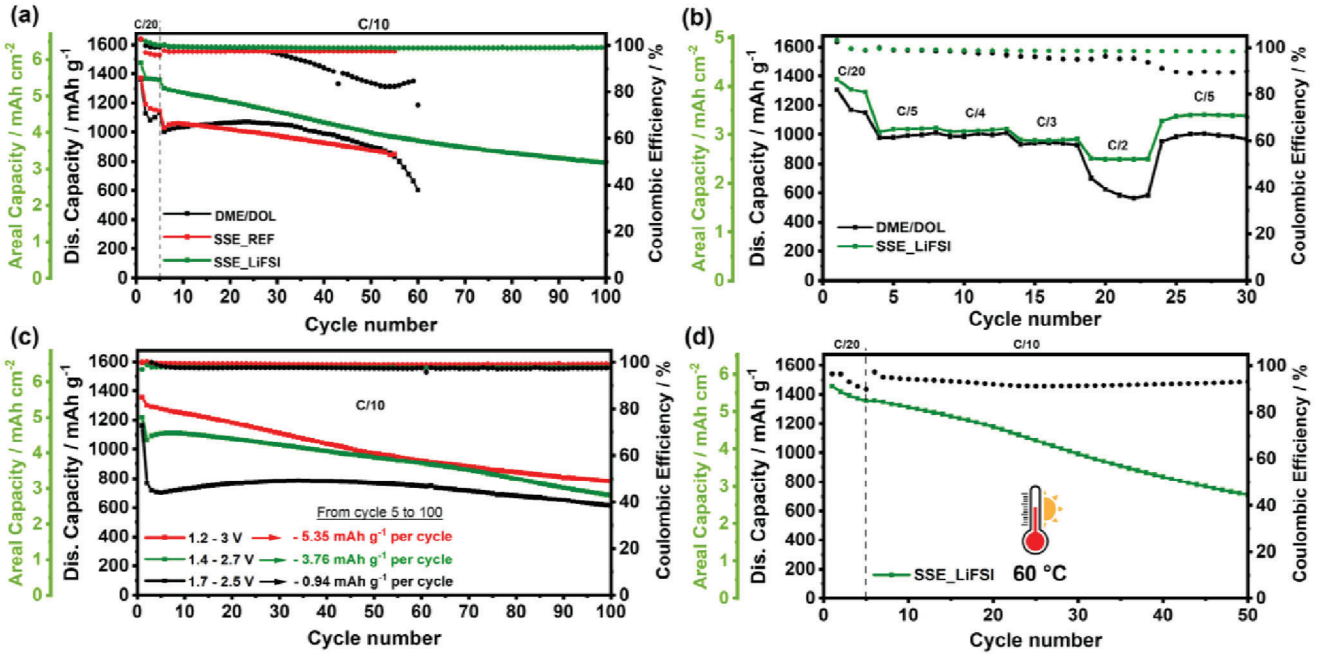

Figure 6. Electrochemical performances of Li-S coin cells. a) Cycling performance of high sulfur loading LSBs using different electrolytes. b) Rate capabilities of Li-S cells using DME/DOL and SSE_LiFSI electrolytes. c) Influence of cut-off voltage on the cycling performance of high sulfur loading LSBs using SSE_LiFSI electrolyte. d) Cycling behavior of LSBs with SSE_LiFSI electrolyte at high temperature (60 °C).

versely, the DME/DOL electrolyte shows lower stability, experiencing short-circuit of the cell at a current density of 3 mA cm^{-2}. Despite the homogeneous lithium deposition presented in the first cycles, this electrolyte shows increasing deposition porosity as previously stated. Moreover, in contrast to the robust LiF-rich SEI layer in the SSE_LiFSI system, the $LiNO_3$ present in the SEI layer formed in the DME/DOL electrolyte is depleted over cycling. This $LiNO_3$ consumption is higher at higher current densities, leading to a weaker SEI layer with subsequent short-circuit of the cell ascribed to Li dendrite formation. Finally, the SSE_REF electrolyte shows the poorest performance, consistent with the earlier observations, displaying the lowest robustness against current due to the porous and fibrillar nature of its depositions.

The electrochemical performance of the proposed electrolytes was further assessed in LSBs using our recently developed high-sulfur loading cathode made up of the ResFArGO 2D graphene-based activated carbon (**Figure 6**a).[26] For all the coin cell cycling experiments, a reduced amount of electrolyte of E/S (electrolyte to sulfur) ratio of 7 µl mg_S^{-1} was established, an adjusted value for this cell configuration to facilitate its eventual upscaling process. Notably, both SSEs demonstrate remarkably high capacities, despite their lower conductivity when compared to the conventional electrolyte. Particularly, it is noteworthy the performance of SSE_LiFSI, which exhibits initial capacity values close to the theoretical ones, suggesting a potential synergistic effect between this type of electrolyte and graphene-based cathodes. This impressive behavior can be attributed to the excellent compatibility between the sulfur cathode and SSEs , which is enabled by the textural properties and surface chemistry of the ResFArGO material. The open and 2D flat-shaped structure of both the ResFArGO carbonaceous material and the high-loading cathode developed shown in Figure S15 (Supporting Information), along with the O-rich functional groups on its surface reported in our previous work,[26] enhances the wettability of the SSEs despite its higher viscosity (as shown Figure S1, Supporting Information) and maximizes sulfur utilization during cycling. The validity of this hypothesis was further reinforced by conducting a parallel LSB cycling experiment without the inclusion of the ResFArGO material, as shown in Figure S16 (Supporting Information). In this case, the DME/DOL electrolyte, which does not encounter wettability issues, demonstrated superior capacity compared to the SSE results. Figure S17 (Supporting Information) provides clear evidence that the presence of the ResFArGO material significantly enhances the wettability of the SSEs, resulting in improved cycling performance.

On the other hand, cyclability is another key parameter influenced by the choice of electrolyte. As shown also in Figure 6a, the SSE_LiFSI electrolyte demonstrates extraordinary LSB stability maintaining a remarkably high and constant CE value of 99% during the analyzed cycles, addressing a known weakness of the technology. In contrast, the DME/DOL electrolyte experienced a continuous CE decrease from cycle 30 and could only withstand 60 cycles due to the depletion of the $LiNO_3$ additive, which plays a pivotal role in cell stability. The success of the anion-selection strategy reflected in the SSE_LiFSI is worth mentioning, as it outstandingly improves both the capacity and, especially, the stability of the Li-S cell. Compared to SSE_REF electrolyte, SSE_LiFSI presents a longer cycle life and improved CE values (96.7% vs 99%, respectively) that are linked with the results obtained above. These results highlight the potential of the SSE_LiFSI electrolyte, demonstrating the advantages of using LiFSI in the electrolyte

composition while discarding SSE_REF due to its poor performance in both lithium symmetric and full-cells.

To further explore the potential of the SSE_LiFSI electrolyte, additional electrochemical characterizations were conducted, including the rate capability study using medium sulfur loading cathodes of 3 mg_S cm^{-2} (Figure 6b; Figure S18, Supporting Information). In comparison to the conventional electrolyte, it has been observed that the performance of SSE_LiFSI is comparable at low C-rates. However, at high C-rates, the SSE_LiFSI presents superior sulfur utilization, achieving significantly higher capacities of 829 mAh g^{-1} at C/2, outperforming the conventional electrolyte. This remarkable cycling rate performance can be attributed to several factors, including the improved Li plating/stripping kinetics, suitable ionic conductivity, and favorable wettability, thus allowing it to outperform the rate capability performance of conventional DME/DOL electrolyte. Furthermore, it is worth noting that the capacity of the cell using SSE_LiFSI electrolyte is consistently recovered when returning to C/5, presenting a stable CE during the entire test. In contrast, while DME/DOL electrolyte can also recover capacity, it shows a clear CE decay due to the consumption of $LiNO_3$ during cycling at high rates. Moreover, the excellent compatibility of the SSE_LiFSI electrolyte at remarkably high cycling rates is further evidenced in its ability to support high sulfur loading long-term cycling at C/5 (Figure S19, Supporting Information). This electrolyte provides remarkable initial high-capacity values of 1200 mAh g^{-1} while providing outstanding cell stability.

Indeed, while the SSE_LiFSI electrolyte has shown promising results, a capacity fading process has been observed during long cycling. To address this issue and further optimize the system, the effect of cut-off voltage on cell performance was studied by analyzing three different voltage ranges: 1.2–3.0, 1.4–2.7, and 1.7–2.5 V. As illustrated in Figure 6c, a wider voltage range leads to higher capacity values (i.e., higher sulfur utilization); however, the capacity drop per cycle is notably more pronounced. Accordingly, the results reflect that a voltage range of 1.7–2.5 V yields the highest capacity retention (80%) after 100 cycles. In contrast, cycling between 1.4 and 2.7 V results in 69% capacity retention, while cycling between 1.2 and 3 V shows 61% retention. However, it should be noted that the 1.7–2.5 V voltage range may not be wide enough, leading to a low and insufficient sulfur utilization of ≈50% (Figure S20a–c, Supporting Information). Therefore, a compromise between sulfur utilization and capacity retention during cycling was sought, thus selecting 1.4–2.7 V as the optimal working voltage range for this system.

The temperature range at which batteries can operate is a crucial parameter for their commercialization. The excellent thermal stability demonstrated by the SSE_LiFSI electrolyte prompts the study of battery cycling at high temperatures (60 °C in this study). As depicted in Figure 6d, the SSE_LiFSI electrolyte exhibits remarkable cycling performance with high-capacity values, evidencing its ability to ensure safe battery cycling even under high-temperature conditions. However, it is worth noting that at 60 °C, the capacity drop is slightly higher, and the CE values are lower compared to RT cycling. Figure S21 (Supporting Information) provides the charge and discharge profiles when cycling at 60 °C. It is evidenced that RT cycling follows a quasi-solid reaction pathway mechanism without clear plateaus, whereas at 60 °C the profiles resemble the dissolution-precipitation reaction pathway typically observed in conventional DME/DOL-based electrolytes, characterized by two distinct plateaus. This change in the voltage profile suggests the presence of soluble polysulfides in the electrolyte due to the increased temperature. This hypothesis has subsequently been confirmed through a polysulfide generation test in the SSE_LiFSI electrolyte. To do this, S_8 and Li_2S were mixed in the electrolyte and stirred at the two cycling temperatures (25 and 60 °C). As shown in Figure S22 (Supporting Information), after several days of reaction, there is minimal coloration at 25 °C. However, at 60 °C, there is a noticeable change in coloration, with the solution turning orange. These results corroborate what was observed in the charge and discharge profiles, demonstrating that increasing the temperature enhances the solubility of these compounds in the electrolyte, thereby modifying the system's conversion mechanism from quasi-solid at room temperature to precipitation-dissolution at 60 °C. Despite these effects, the SSE_LiFSI electrolyte demonstrates good properties for ensuring safe cycling even at high temperatures, although some modifications may be considered to address the new challenges posed.

To validate the practical application of the SSE_LiFSI electrolyte, a high sulfur loading (4 mg_S cm^{-2}) prototype Li-S pouch cell was assembled and tested. In this case, the same E/S ratio of 7 µl mg_S^{-1} established for the coin cells was employed due to the acknowledged presence of more pronounced dead space in the monolayer pouch cell configuration when compared to the multilayer pouch cell design. **Figure 7a** demonstrates that the performance trend observed in the coin cell results is consistent in the larger pouch cells. The conventional DME/DOL electrolyte presents a limited cycling stability of only 20 cycles. Beyond this point, the consumption of $LiNO_3$ results in a decrease in both capacity and CE due to its diminished ability to protect the lithium anode until the cell eventually fails. Furthermore, as illustrated in Figure 7b, an increased polarization of the cell is observed due to the high LiPS solubility of this electrolyte. However, the stability of the Li-S pouch cell using SSE_LiFSI electrolyte is significantly improved due to the robust and effective LiF-rich protective SEI layer formed on the Li anode, enabling a minimum of 100 cycles (over five times higher compared to those of the conventional electrolyte) while maintaining a stable CE high value of 99%. Notably, this CE value is slightly superior to that achieved during coin cell cycling, which reached a value of 98%. This slight improvement observed in the CE of the prototype cell may be attributed to the application of external stacking pressure, a factor demonstrated to exert a remarkable and beneficial influence on LMB performance by enhancing Li deposition behavior and morphology.[54,55] In addition, the SSE_LiFSI electrolyte exhibits excellent sulfur utilization, leading to a remarkably high capacity of 93 mAh (4.6 mAh cm^{-2}) at C/10, with an impressive capacity retention of 70% after 100 cycles. Moreover, it presents smooth one-single charge/discharge profiles (Figure 7c), which are characteristic of quasi-solid reaction pathways associated with the use of SSE. These results highlight the effectiveness of the holistic Li-S battery approach and pave the way for the development of high-performing LSBs suitable for practical applications.

Despite the progress made in this manuscript, there is still room for improvement. Through the approach proposed during this study, the scaling of the system has been achieved, obtaining an average Coulombic Efficiency of 99.0% at moderate C-rates

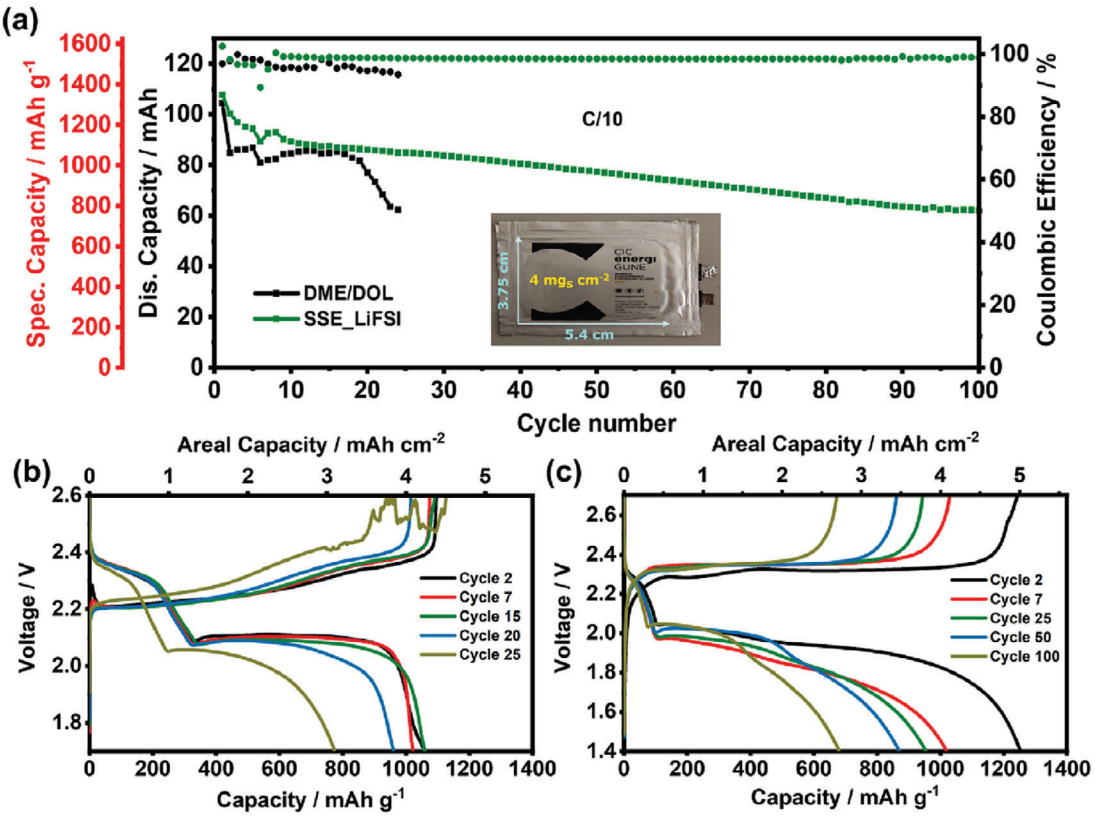

Figure 7. Electrochemical cycling performance of LSB pouch cells. a) Total and specific capacities of the pouch cells using DME/DOL and SSE_LiFSI electrolytes. Pouch cell voltage profile comparison between b) DME/DOL and c) SSE_LiFSI electrolytes.

such as C/10 that must be enhanced with the aim of approaching more realistic scenarios, close to their future industrial application. Therefore, a further improvement in the stability of the LMA is needed, either through an enhancement in its quality, protection by means of an ex-situ SEI layer, or a combination of both approaches.

3. Conclusion

This work demonstrates the successful implementation of a holistic LSB approach by combining a high-performing 2D graphene-based sulfur cathode with a well-suited SSE in the final battery design. Due to the importance of anion selection for the generation of a suitable SEI layer, LiFSI salt was included in the SSE formulation resulting in the construction of a robust and effective LiF-rich SEI protective layer on the LMA. Consequently, the SSE_LiFSI electrolyte exhibits outstanding compatibility with lithium metal, achieving a high CE of 98.8% in the Li||Cu test, facilitating a compact, thin, and dense lithium deposition, and offering an excellent current density tolerance. Notably, SSE_LiFSI electrolyte presents a non-flammable nature, ensuring the safety of the battery system by mitigating the fire hazard compared to the conventional electrolyte. In terms of LSB performance, the holistic strategy demonstrates an unprecedented symbiotic effect, significantly improving cell stability and sulfur utilization compared to the conventional electrolyte and SSE_REF. In addition, the scalability of this new battery system is successfully demonstrated in a 20 cm^2 monolayer prototype cell, yielding outstanding cycling stability and achieving a fivefold increase in cycle life compared to the conventional electrolyte. The cell delivers a high total capacity of 94 mAh at C/10, with a remarkable capacity retention of 70% after 100 cycles and a high average CE of 99.0%. This study highlights the applicability of the holistic battery concept as a cornerstone in paving the way toward the commercialization of high energy density, safe, and long cycle life LSBs.

Supporting Information

Supporting Information is available from the Wiley Online Library or from the author.

Acknowledgements

J.C. is a beneficiary of the Predoctoral Program from the Education Department of the Basque Government. The authors want to acknowledge GRAPHENEA for supplying graphene oxide. Chunmei Li is acknowledged for fruitful discussion. Hegoi Manzano at the University of the Basque Country is thanked for providing technical advice and access to facilities throughout computational work. This work was funded by the European Union's Horizon 2020 research and innovation program Graphene Flagship Core Project 3 (GrapheneCore3) under grant agreement 881603.

Conflict of Interest

The authors declare no conflict of interest.

Data Availability Statement

Research data are not shared.

Keywords

2D graphene-based sulfur cathodes, electrolyte additives, electrolyte engineering, lithium metal anodes, lithium-sulfur batteries, pouch cells, solid electrolyte interphases

Received: July 24, 2023
Revised: October 9, 2023
Published online: November 13, 2023

[1] H. Zhang, G. G. Eshetu, X. Judez, C. Li, L. M. Rodriguez-Martínez, M. Armand, *Angew. Chem., Int. Ed.* **2018**, *57*, 15002.
[2] J. Liu, Z. Bao, Y. Cui, E. J. Dufek, J. B. Goodenough, P. Khalifah, Q. Li, B. Y. Liaw, P. Liu, A. Manthiram, Y. S. Meng, V. R. Subramanian, M. F. Toney, V. V. Viswanathan, M. S. Whittingham, J. Xiao, W. Xu, J. Yang, X.-Q. Yang, J.-G. Zhang, *Nat. Energy* **2019**, *4*, 180.
[3] C. P. Grey, D. S. Hall, *Nat. Commun.* **2020**, *11*, 2.
[4] S. Yuan, K. Ding, X. Zeng, D. Bin, Y. Zhang, P. Dong, Y. Wang, *Adv. Mater.* **2023**, *35*, 2206228.
[5] J. T. Frith, M. J. Lacey, U. Ulissi, *Nat. Commun.* **2023**, *14*, 420.
[6] X. Peng, Y. Lin, Y. Wang, Y. Li, T. Zhao, *Nano Energy* **2022**, *96*, 107102.
[7] B. Liu, J. G. Zhang, W. Xu, *Joule* **2018**, *2*, 833.
[8] Z. Yang, H. Huang, F. Lin, *Adv. Energy Mater.* **2022**, *12*, 2200383.
[9] S. Dörfler, S. Walus, J. Locke, A. Fotouhi, D. J. Auger, N. Shateri, T. Abendroth, P. Härtel, H. Althues, S. Kaskel, *Energy Technol.* **2021**, *9*, 2000694.
[10] Y. Jin, K. Liu, J. Lang, X. Jiang, Z. Zheng, Q. Su, Z. Huang, Y. Long, C.-A. Wang, H. Wu, Y. Cui, *Joule* **2020**, *4*, 262.
[11] J. B. Robinson, K. Xi, R. V. Kumar, A. C. Ferrari, H. Au, M.-M. Titirici, A. Parra-Puerto, A. Kucernak, S. D. S. Fitch, N. Garcia-Araez, Z. L. Brown, M. Pasta, L. Furness, A. J. Kibler, D. A. Walsh, L. R. Johnson, C. Holc, G. N. Newton, N. R. Champness, F. Markoulidis, C. Crean, R. C. T. Slade, E. I. Andritsos, Q. Cai, S. Babar, T. Zhang, C. Lekakou, N. Kulkarni, A. J. E. Rettie, R. Jervis, et al., *J. Phys. Energy* **2021**, *3*, 031501.
[12] S. Dörfler, H. Althues, P. Härtel, T. Abendroth, B. Schumm, S. Kaskel, *Joule* **2020**, *4*, 539.
[13] P. Brooks, *Lithium Sulfur Batter*, John Wiley & Sons, Ltd, New Jersey, USA **2019**, 293.
[14] M. Zhao, B.-Q. Li, X.-Q. Zhang, J.-Q. Huang, Q. Zhang, *ACS Cent. Sci.* **2020**, *6*, 1095.
[15] G. Jiménez-Martín, J. Castillo, X. Judez, J. L. Gómez-Urbano, G. Moreno-Fernández, A. Santiago, A. Saenz De Buruaga, I. Garbayo, J. A. Coca-Clemente, A. Villaverde, M. Armand, C. Li, D. Carriazo, *Batteries Supercaps* **2022**, *5*, 202200167.
[16] A. Manthiram, Y. Fu, S.-H. Chung, C. Zu, Y.-S. Su, *Chem. Rev.* **2014**, *114*, 11751.
[17] T. Lei, W. Chen, W. Lv, J. Huang, J. Zhu, J. Chu, C. Yan, C. Wu, Y. Yan, W. He, J. Xiong, Y. Li, C. Yan, J. B. Goodenough, X. Duan, *Joule* **2018**, *2*, 2091.
[18] G. Li, W. Lei, D. Luo, Y. Deng, Z. Deng, D. Wang, A. Yu, Z. Chen, *Energy Environ. Sci.* **2018**, *11*, 2372.
[19] Z. Wei Seh, W. Li, J. J. Cha, G. Zheng, Y. Yang, M. T. Mcdowell, P.-C. Hsu, Y. Cui, *Nat. Commun.* **2013**, *4*, 1331.
[20] T. Li, X. Bai, U. Gulzar, Y.-J. Bai, C. Capiglia, W. Deng, X. Zhou, Z. Liu, Z. Feng, R. Proietti Zaccaria, *Adv. Funct. Mater.* **2019**, *29*, 1901730.
[21] H. J. Peng, J. Q. Huang, X. B. Cheng, Q. Zhang, *Adv. Energy Mater.* **2017**, *7*, 1700260.
[22] Y. Ge, Z. Chen, S. Ye, Z. Zhu, Y. Tu, X. Yang, *J. Mater. Chem. A* **2018**, *6*, 14885.
[23] H. Yang, X. Zhang, J. Guo, W. Zhu, S. Zhao, F. Wang, Q. Fan, H. Xiao, F. Zhang, *J. Alloys Compd.* **2018**, *768*, 495.
[24] R. Lu, M. Cheng, L. Mao, M. Zhang, H. Yuan, K. Amin, C. Yang, Y. Cheng, Y. Meng, Z. Wei, *EcoMat* **2020**, *2*, e12010.
[25] Y. Xiang, L. Lu, A. G. P. Kottapalli, Y. Pei, *Carbon Energy* **2022**, *4*, 346.
[26] J. Castillo, A. Santiago, X. Judez, J. A. Coca-Clemente, A. Saenz De Buruaga, J. L. Gómez-Urbano, J. A. González-Marcos, M. Armand, C. Li, D. Carriazo, *ACS Appl. Energy Mater.* **2023**, *6*, 3579.
[27] X.-B. Cheng, C. Yan, J.-Q. Huang, P. Li, L. Zhu, L. Zhao, Y. Zhang, W. Zhu, S.-T. Yang, Q. Zhang, *Energy Storage Mater.* **2017**, *6*, 18.
[28] A. Fotouhi, D. J. Auger, L. O'Neill, T. Cleaver, S. Walus, *Energies* **2017**, *10*, 1937.
[29] J. Sun, T. Wang, Y. Gao, Z. Pan, R. Hu, J. Wang, *InfoMat* **2022**, *4*, e12359.
[30] L.-P. Hou, X.-Q. Zhang, N. Yao, X. Chen, B.-Q. Li, P. Shi, C.-B. Jin, J.-Q. Huang, Q. Zhang, *Chem* **2022**, *8*, 1083.
[31] H. Ye, Y. Li, *Nano Res. Energy* **2022**, *1*, e9120012.
[32] Y. Liu, Y. Elias, J. Meng, D. Aurbach, R. Zou, D. Xia, Q. Pang, *Joule* **2021**, *5*, 2323.
[33] C. Kensy, F. Schwotzer, S. Dörfler, H. Althues, S. Kaskel, *Batteries Supercaps* **2021**, *4*, 823.
[34] Q. Cheng, Z.-X. Chen, X.-Y. Li, L.-P. Hou, C.-X. Bi, X.-Q. Zhang, J.-Q. Huang, B.-Q. Li, *J. Energy Chem.* **2023**, *76*, 181.
[35] F. Y. Fan, Y.-M. Chiang, *J. Electrochem. Soc.* **2017**, *164*, A917.
[36] J. Liu, S. Li, M. Marium, B. Wang, K. Ueno, K. Dokko, M. Watanabe, *Sustainable Energy Fuels* **2021**, *5*, 1821.
[37] X. Cao, P. Gao, X. Ren, L. Zou, M. H. Engelhard, B. E. Matthews, J. Hu, C. Niu, D. Liu, B. W. Arey, C. Wang, J. Xiao, J. Liu, W. Xu, J. G. Zhang, *Proc. Natl. Acad. Sci. U. S. A.* **2021**, *118*, e2020357118.
[38] L. Kong, L. Yin, F. Xu, J. Bian, H. Yuan, Z. Lu, Y. Zhao, *J. Energy Chem.* **2021**, *55*, 80.
[39] L. Cheng, L. A. Curtiss, K. R. Zavadil, A. A. Gewirth, Y. Shao, K. G. Gallagher, *ACS Energy Lett.* **2016**, *1*, 503.
[40] C. Zhu, C. Sun, R. Li, S. Weng, L. Fan, X. Wang, L. Chen, M. Noked, X. Fan, *ACS Energy Lett.* **2022**, *7*, 1338.
[41] Z. Xu, K. Deng, S. Zhou, D. Mo, *J. Power Sources* **2023**, *559*, 232631.
[42] X. Feng, Z. Zhang, R. Li, W. Xiong, B. Yu, M. Wang, J. Chen, Z. Ma, B. Guo, Y. Huang, X. Li, *Sustainaible Energy Fuels* **2022**, *6*, 2198.
[43] J. Castillo, J. A. Coca-Clemente, J. Rikarte, A. Sáenz De Buruaga, A. Santiago, C. Li, *APL Mater.* **2023**, *11*, 010901.
[44] Q. Liu, Y. Liu, Z. Chen, Q. Ma, Y. Hong, J. Wang, Y. Xu, W. Zhao, Z. Hu, X. Hong, J. Wang, X. Fan, H. B. Wu, *Adv. Funct. Mater.* **2023**, *33*, 2209725.
[45] X. Cao, H. Jia, W. Xu, J.-G. Zhang, *J. Electrochem. Soc.* **2021**, *168*, 010522.
[46] Y. Chen, M. Li, Y. Liu, Y. Jie, W. Li, F. Huang, X. Li, Z. He, X. Ren, Y. Chen, X. Meng, T. Cheng, M. Gu, S. Jiao, R. Cao, *Nat. Commun.* **2023**, *14*, 2655.
[47] J.-X. Guo, W.-B. Tang, X. Xiong, H. Liu, T. Wang, Y. Wu, X.-B. Cheng, *Front. Chem. Sci. Eng.* **2023**, *17*, 1354.
[48] X. Cao, L. Zou, B. E. Matthews, L. Zhang, X. He, X. Ren, M. H. Engelhard, S. D. Burton, P. Z. El-Khoury, H.-S. Lim, C. Niu, H. Lee, C.

Wang, B. W. Arey, C. Wang, J. Xiao, J. Liu, W. Xu, J.-G. Zhang, *Energy Storage Mater.* **2021**, *34*, 76.
[49] J. Moon, D. O. Kim, L. Bekaert, M. Song, J. Chung, D. Lee, A. Hubin, J. Lim, *Nat. Commun.* **2022**, *13*, 4538.
[50] T. Zheng, B. Zhu, J. Xiong, T. Xu, C. Zhu, C. Liao, S. Yin, G. Pan, Y. Liang, X. Shi, H. Zhao, R. Berger, Y.-J. Cheng, Y. Xia, P. Müller-Buschbaum, *Energy Storage Mater.* **2023**, *59*, 102782.
[51] J. Fu, X. Ji, J. Chen, L. Chen, X. Fan, D. Mu, C. Wang, *Angew. Chem., Int. Ed.* **2020**, *132*, 22194.
[52] M. Martinez-Ibañez, N. Boaretto, L. Meabe, X. Wang, H. Zhu, A. Santiago, O. Zugazua, M. Forsyth, M. Armand, H. Zhang, *Chem. Mater.* **2022**, *34*, 7493.
[53] B. D. Adams, J. Zheng, X. Ren, W. Xu, J.-G. Zhang, *Adv. Energy Mater.* **2018**, *8*, 1702097.
[54] C. Fang, B. Lu, G. Pawar, M. Zhang, D. Cheng, S. Chen, M. Ceja, J.-M. Doux, H. Musrock, M. Cai, B. Liaw, Y. S. Meng, *Nat. Energy* **2021**, *6*, 987.
[55] F. Dai, M. Cai, *Commun. Mater.* **2022**, *3*, 64.